Heterogeneous Growth of UiO-66-NH₂ on Oxidized Single-Walled Carbon Nanotubes to Form "Beads-on-a-String" Composites

Zidao Zeng,[†] Dan C. Sorescu,^{‡,§} David L. White,[†] Sean I. Hwang,[†] Wenting Shao,[†] Xiaoyun He,[†] Zachary M. Schulte,[†] Nathaniel L. Rosi,^{†,§} and Alexander Star*,^{†,||}

Department of Chemistry, University of Pittsburgh, Pittsburgh, Pennsylvania 15260, United States

KEYWORDS: density functional theory, graphene, metal-organic frameworks, organophosphorus compounds, sensors.

ABSTRACT: In this work we demonstrate a facile synthesis of UiO-66-NH $_2$ metal-organic framework (MOF)/oxidized single-walled carbon nanotubes (ox-SWCNTs) composite at room temperature. Acetic acid (HAc) was used as a modulator to manipulate the morphology of the MOF in these composites. With zirconium oxide-cluster (Zr) to 2-aminoteraphthalate linker (ATA) 1: 1.42 ratio and acetic acid modulator, we achieved predominately heterogeneous MOF growth on the sidewalls of CNTs. Understanding the growth mechanism of these composites was facilitated by conducting DFT calculations to investigate the interactions between ox-SWCNTs and the MOF precursors. The synthesized composites combine both micro-porosity of the MOF and electrical conductivity of the SWCNTs. Gas sensing tests demonstrated higher response for UiO-66-NH $_2$ /ox-SWCNT hybrid toward dry air saturated with dimethyl methylphosphonate (DMMP) vapor compared to oxidized single-walled carbon nanotubes (ox-SWCNTs) alone.

■ INTRODUCTION

Metal-organic frameworks (MOFs) are known for their high porosity and large surface area. They have been studied and applied in many fields such as gas storage, separation and catalysis. Most MOFs are not electrically conductive due to the lack of free charge carriers or low-energy transfer pathways in their structures, thus limiting their applications where electrical properties are desired. Extensive research has been conducted to explore the synthesis of conductive MOFs. However, for such conductive MOFs, the achieved electrical conductivity is significantly lower as compared to traditional solid state materials. A promising approach to synthesize conductive MOFs is to hybridize them with conductive nanocarbon materials like carbon nanotubes (CNTs).

Core-shell MOF decoration on multi-walled carbon nanotubes (MWCNTs) was first reported by Shim *et al.*⁴ The hybridization of MWCNTs and MOFs enables development of several applications in electrical related areas such as electrolysis, energy storage, supercapacitor, and electrochemical sensing using MOFs.⁵⁻¹⁰ Single-walled carbon nanotubes (SWCNTs) were first successfully hybridized with MIL-101 by adding SWCNTs into MOF precursor mixture.¹¹ A hydrogen storage improvement relative to pure MOF ranging from 6.37 to 9.18 wt% was achieved by these composites.

SWCNTs were used as templates for the growth of HKUST-1.¹² The involvement of SWCNTs significantly altered the morphology of HKUST-1 and the resulting composites had enhanced capacity to capture CO₂ due to a higher surface area. Unlike metallic MWCNTs, SWCNTs can be either metallic or semiconducting based on their chirality.¹³ Semiconducting SWCNTs are sensitive to their local chemical environment as their electronic structure can be easily perturbed by dopants.¹⁴ Embedding SWCNTs into MOFs opens the possibility to use these hybrid systems in chemical sensing applications. Furthermore, combining SWCNT with MOF structures provides an opportunity to expand the class of conductive MOFs without limiting MOF variety.

We have previously synthesized ZIF-8/SWCNT composites which are microporous and conductive with promising applications in chemiresistive sensing. We demonstrated that ZIF-8 growth on SWCNT sidewalls was facilitated by the molecular ordering of 2-methylimidazole (2mIM) precursor on the surface of SWCNTs via non-covalent pi-pi stacking. In the interest of developing a general synthetic methodology for MOF-SWCNT composites and to achieve better electronic coupling between the components, in this work we investigated covalent attachment of MOFs to oxygen-containing functional groups of SWCNTs. As a model system we

[†]National Energy Technology Laboratory, United States Department of Energy, Pittsburgh, Pennsylvania 15236, United States

 $^{^{\}S}Department\ of\ Chemical\ and\ Petroleum\ Engineering,\ University\ of\ Pittsburgh,\ Pennsylvania\ 15261,\ United\ States$

 $^{{}^{\}parallel} Department \ of \ Bioengineering, \ University \ of \ Pittsburgh, \ Pennsylvania \ 15261, \ United \ States$

selected UiO-66-NH₂ MOFs and investigated their nucleation and growth on oxidized single-walled carbon nanotubes (ox-SWCNTs).

UiO-66-NH2 is composed of zirconium oxide-cluster secondary building units (SBU) and 2-aminoterephtahlate linkers (ATA). Previous studies revealed CO2 and NO2 gas removal as potential applications for UiO-66-NH2.16,17 Two UiO-66-NH2/MWCNT composites have been synthesized for applications of dye separation and electrocatalytic sensing. 18,19 However, composites consisting of UiO-66-NH₂ and SWCNT have not been reported. In this work, we present the synthesis of room-temperature UiO-66-NH₂ MOF assembly on the surface of commercial ox-SWCNTs with 3 atomic percent of oxygen-containing functional groups. Hydroxyl and carboxyl groups on the sidewalls and termini of ox-SWCNTs serve as anchors for zirconium oxide-clusters. The synthesis features a controlled MOF nucleation to form a "beads-on-a-string" morphology without introducing external template molecules on ox-SWCNTs. DFT calculations were conducted to provide a fundamental understanding of the initial energetics steps involved in MOF nucleation. The assynthesized composites were used to fabricate FET transistors, and chemiresistive sensing experiments toward DMMP were performed.

■ EXPERIMENTAL SECTION

Chemicals. Ox-SWCNT (P3-SWNT, Carbon Solutions, Inc), zirconium(IV) propoxide solution (70 wt. % in 1-propanol) (Sigma-Aldrich), 2-aminoterephthalic acid (Alfa Aesar), N,N-dimethylformamide (Fisher Scientific), glacial acetic acid (Macron Fine Chemicals), and ethanol (Decon Labs) were purchased and used without further purification.

Preparation of Zr oxide-cluster stock solution. 7 mL of N,N-dimethylformamide (DMF) was mixed with 4 mL of glacial acetic acid which was followed by 71 μ L of 70% zirconium propoxide [Zr(OnPr)₄] solution in 1-propanol. The resulting mixture was heated in an oven at 130 °C for 2 hours until the solution appeared yellow color. The mixture was then allowed to cool to room temperature. [Zr] = 14.4 mM for the stock solution.

Preparation of ATA stock solution. To 2.4 mL of DMF solution, 40.76 mg of ATA powder was added. [ATA] = 93.6 mM for the stock solution.

Synthesis of UiO-66-NH₂. UiO-66-NH₂ was synthesized following a published procedure. ²⁰ The Zr oxide-cluster stock solution and ATA solution were mixed at fixed ratios (Table S1). The mixture was stirred for 20 h at room temperature. The resulting MOF crystals were separated by centrifugation. As-obtained MOF was washed with DMF twice and subsequently with ethanol twice and was stored in ethanol.

Preparation of ox-SWCNTs stock suspension. 5 mg of ox-SWCNTs were added to 10 mL of DMF. The mixture was sonicated in a bath sonicator for one hour to form a uniform black suspension. The suspension was sonicated for 15 min before ox-SWCNTs were used for each synthesis.

Synthesis of UiO-66-NH₂/ox-SWCNT. The desired amount of ox-SWCNTs stock suspension was added to MOF precursor solutions as described in Table S1. The mixture underwent the same synthetic procedure as UiO-66-NH₂ MOF and was separated and stored

in the same manner. Procedure details are provided in supporting information.

Fabrication of FET and chemiresistor devices. A prefabricated $2\times 2\,\text{mm}^2\,\text{Si}/\text{SiO}_2$ chip with four interdigitated gold electrodes was used to fabricate the devices. When drop-casting, devices were heated to 200 °C then 5 μL of sample suspension was drop-cast on the surface to dry. When using dielectrophoresis (DEP), a Keithley 3390 Arbitrary Waveform Generator was used to generate a sine wave (10 Vpp, 10 MHz). 5 μL of sample suspension was drop-cast on the device and the sine wave was applied to the electrodes for 2 min. Both drop-cast and DEP devices were washed with water and then annealed at 200 °C for 1 hour to remove any solvent residue.

■ RESULTS AND DISCUSSION

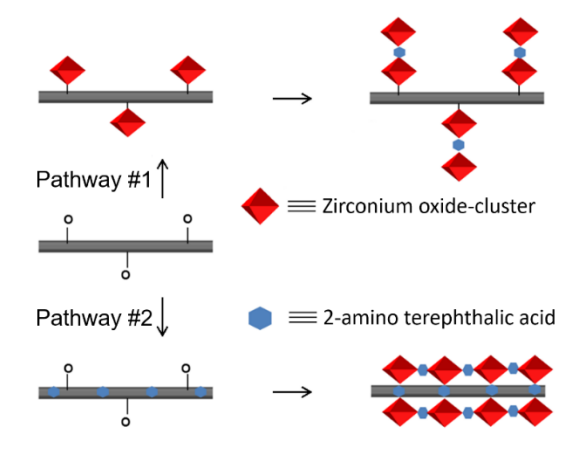


Figure 1. Schematic representation of UiO-66-NH₂/ox-SWCNT composites synthetic pathways.

When CNTs are introduced to MOF synthesis, there are two reaction environments, i.e. solution and ox-SWCNT surface. MOF can nucleate both homogeneously in solution and heterogeneously on the surface of ox-SWCNTs. During homogeneous nucleation, ox-SWCNTs would be wrapped by growing MOF aggregates resulting in a morphology characterized by bundles of ox-SWCNT embedded in large MOF aggregates. Alternatively, when MOF nanoparticles start nucleating from the sidewalls of ox-SWCNTs, the material would have a morphology of crystalline beads threaded by ox-SWCNTs. Two general pathways for heterogeneous UiO-66-NH₂ nucleation are depicted in Figure 1. In zirconium oxide-cluster anchored pathway (pathway #1), Zr oxide-clusters react with the carboxylic groups on the sidewalls of ox-SWCNTs. The covalently attached clusters serve as nucleation sites to grow the MOF structure. In linker-anchored pathway (pathway #2), 2-aminoterephthalic acid (ATA) molecules noncovalently interact with ox-SWCNT sidewalls via pi-pi stacking and template the MOF growth.

Table 1. Synthesis parameters for UiO-66-NH₂/ox-SWCNT

Materials	[Zr] (mM)	Vial	Syringe pump	Zr : Acetic acid (Molar Ratio)
1	11.3	ATA + Zr		1:442
2	1.13	ATA + Zr		1:442

3	1.13	Zr	ATA	1:442
4	1.13	ATA	Zr	1:442
5	1.13	ATA + Zr		1: 884
6	1.13	Zr	ATA	1:884
7	1.13	ATA	Zr	1:884
8	1.13	ATA + Zr		1:1326

Zr:ATA ratio (mmol: mmol) is 1:1.42 for all the syntheses. Ox-SWCNTs amount is $158~\mu g$ for all the syntheses.

Exploration of the relevant synthetic pathways was conducted through a series of different synthetic conditions. First, a one-pot synthesis (SI Experimental section) where ox-SWCNTs were directly mixed with MOF precursors produced the product (material 1 in Table 1). For the resulting material, large MOF aggregates were observed under TEM (Figure S1A). The XRD pattern confirmed the crystal structure in material 1 as UiO-66-NH₂ (Figure S1C). The large MOF aggregation revealed homogeneous MOF growth in the one-pot synthesis. ox-SWCNTs failed to template heterogeneous MOF nucleation when they were simply mixed with MOF precursors. Moreover, less exposed ox-SWCNTs in material 1 failed to form a conducting carbon nanotube network. Devices fabricated from drop-casting material 1 were not conductive.

To successfully hybridize UiO-66-NH₂ with ox-SWCNTs into electrically conductive composites, understanding how MOF precursors interact with ox-SWCNT sidewalls is essential. For this purpose, first principles density functional theory (DFT) calculations were conducted to analyze the early steps of the MOF nucleation on the ox-SWCNT sidewalls. Additional details of the computational methods used are provided in supporting information section.

The first objective of these DFT calculations was to probe the modification of the adsorption properties of ATA molecule and Zr₆O₄(OH₄)(CH₃COO)₁₂ cluster (hereafter denoted as Zr(CL)) as representative precursors in UiO-66-NH2 synthesis on the ox-SWCNTs. In this work, the ox-SWCNTs were represented by a (14,0) SWCNT model. This analysis has been done both for the case of a pristine SWCNT and for a defective SWCNT containing a Stone-Wales defect functionalized with two COOH and O groups, respectively. The corresponding results are shown in Figures S2 and S3. As seen from these figures, interaction of ATA and Zr(CL) to an unmodified SWCNT is governed by van der Waals interactions. The binding energies are 13.9 kcal/mol for ATA and 16.6 kcal/mol for Zr(CL). In this case, ATA molecule adsorbs flat on nanotube surface while Zr(CL) adopts a position which maximizes the attractive interactions with C atoms of the nanotube. In particular, in the most favorable binding configuration (panel d in Figure S3) the 4 CH₃COO groups of Zr(CL) are oriented sideways relative to CNT axis instead of pointing down directly toward the SWCNT surface (as seen in panels b and c in Figure S3). In the presence of a functionalized defect on SWCNT surface, adsorption energies of both molecular systems increase to maximum values of 21.4 kcal/mol for ATA and 20.2 kcal/mol for Zr(CL), respectively. The higher interaction in this case is due to formation of additional attractive hydrogen bonds to the COOH group at the defect site, while maximizing the van der Waals interactions with the C atoms of the nanotube support. Even larger increases of adsorption energies to values of about 31-32 kcal/mol are seen when co-adsorption of ATA and Zr(CL) takes place near the defect site, independent on the relative order of these two systems from the defect site (panels g and h in Figure S3). These results indicate that the sidewalls of SWCNT and more importantly the functionalized defects on SWCNT surface can act as attractive sites for ATA and Zr(CL) precursors, leading to an increase in their concentration on nanotube surface and facilitating their mutual interaction.

Another aspect investigated theoretically is related to the energetic properties of representative configurations that might be involved in the early nucleation steps of UiO-66-NH $_2$ on the sidewalls of SWCNT, particularly in the interface region of Zr(CL)-ATA with SWCNT. Sequences of corresponding intermediates are presented in **Figure 2**, both for the case when Zr(CL) interacts first directly with the COOH at the defect site followed by interactions with three ATA molecules (panels a-e) or when Zr(CL) interacts successively with up to three ATA molecules, one of which being hydrogen bonded to a functionalized defect site (panels f-i). For both sequences of steps the

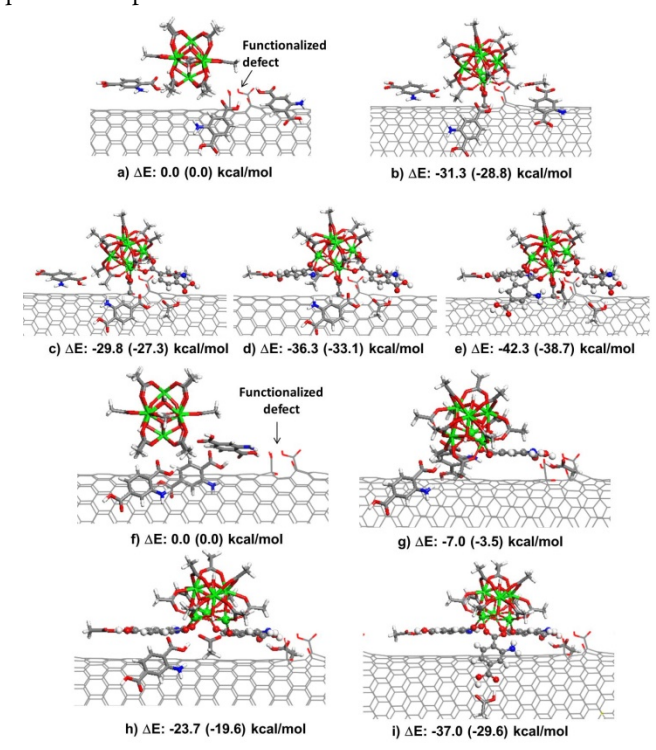


Figure 2. Representative molecular configurations involved in the early nucleation steps of UiO-66-NH $_2$ on the sidewalls of SWCNT. Panels (a-e) correspond to the case when a Zr(CL) adsorbs near a functionalized defect on SWCNT surface followed by successive reactions with up two three ATA molecules while panels (f-i) indicate the case when adsorption of Zr(CL) is mediated by an ATA molecule to the same type of defect site followed by reactions with up to three ATA molecules. The indicated numerical values represent the relative energies taken with respect to the reference configuration (a) for (a-e) panels and respectively (f) for (f-i) panels. The corresponding values obtained by inclusion of solvation effects are indicated in parentheses. For increased visibility the COO group at the defect site (for panels b-e) and ATA molecules coupled to Zr-oxide (panels (b-e) and (g-i)) are shown using ball and stick models (versus a stick diagram before coupling). Similarly, the atoms of

the Zr-oxide are represented using a stick diagram excepting the Zr atoms coupled either with ATA or COO which are represented using ball and stick models. All the other atoms are shown using a line representation. The coloring scheme used is C (gray), O (red), N (blue), H (white), and Zr (green).

initial state corresponds to Zr(CL) and three ATA molecules co-adsorbed on SWCNT surface. Anchoring of Zr-cluster to the defect via the COO group (panel b in Figure 2) upon reaction of Zr(CL) with

COOH at the defect site and with formation of a co-adsorbed CH₃COOH molecule (hereafter abbreviated as AA) leads to a stabilization by 31.3 kcal/mol relative to initial starting state (panel a in Figure 2), indicating a favorable energetic process. From this reacted state the resulted Zr-oxide cluster (Zr(CL,r)) can further react with one (panel c), two (panel d) and respectively three ATA molecules (panel e in Figure 2), with formation of one, two and respectively three AA molecules

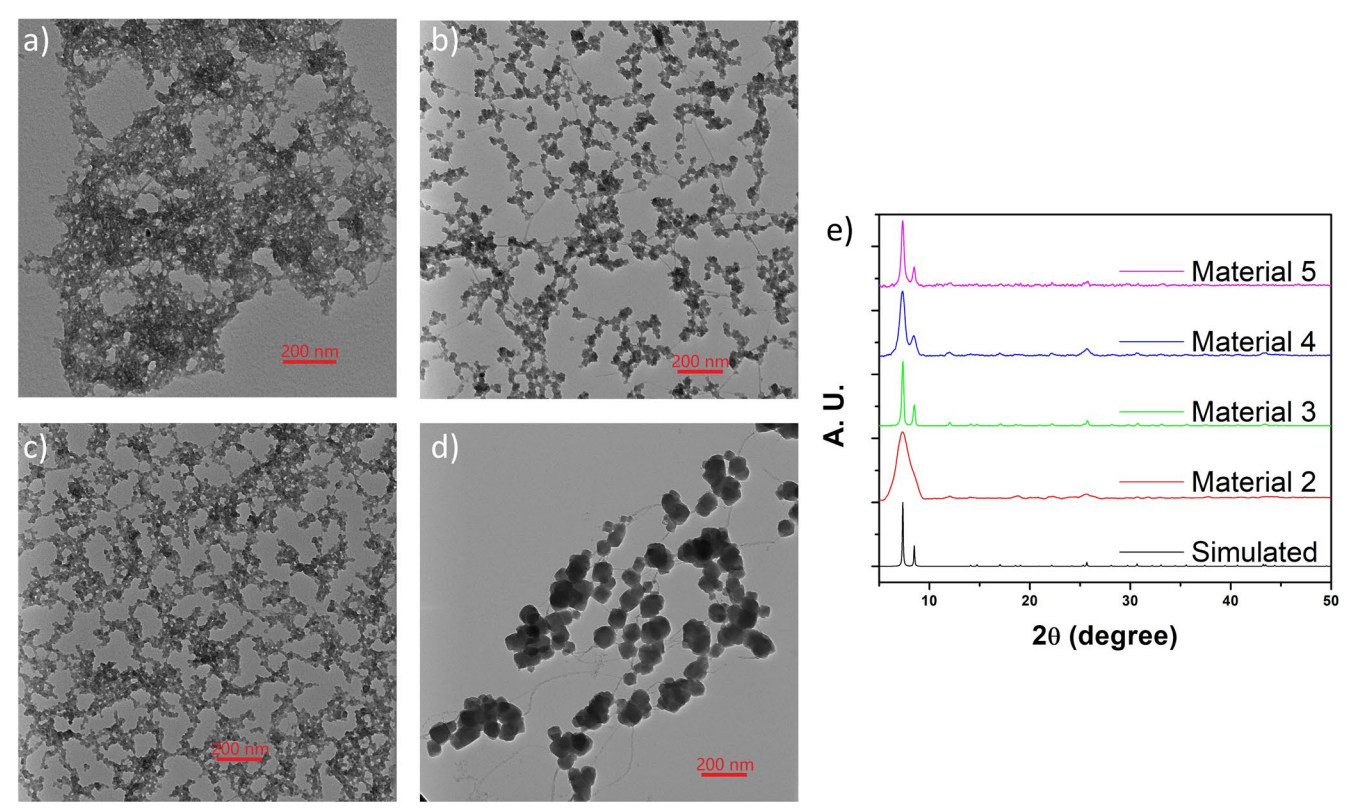


Figure 3. TEM images of materials 2 (a), 3 (b), 4 (c), and 5 (d). e) XRD patterns of materials 2 (red), 3 (green), 4 (blue), 5 (magenta) and simulated bulk UiO-66-NH₂ (black)

adsorbed on nanotube surface. In each of these processes, upon H elimination, the ATA molecules become fused to a pair of Zr atoms of the Zr-oxide cluster. Each of these sequential reaction steps are exothermic relative to the initial state and overall, the final state, corresponding to three ATA molecules becoming fused to Zr(CL,r) and co-adsorbed with three AA molecules (panel e in Figure 2), is energetically the most stable. These findings are similar to those found for the sequence of configurations f)-i). Specifically, for this second sequence of states, the reaction is initiated from Zr(CL) co-adsorbed with three other ATA molecules among which one is hydrogen bonded to the COOH group of the defect. Upon interaction of Zr(CL) with one (panel g), two (panel h) and respectively three (panel i) ATA molecules, these become fused to the Zr cluster while the resulted AA molecules remain adsorbed on CNT surface. As shown in panels g-i in Figure 2, all intermediate steps are exoenergetic relative to the initial starting configuration and the final state is again energetically the most stable. These findings indicate that independent of the sequence of individual steps, both pathways are energetically favorable. We note that this analysis should be considered

only as a qualitative description of the initial nucleation steps that might be involved, as it does not include data about transition states that might be involved in formation of various intermediates, or data about entropic or vibrational energy contributions that might arise from formation of various species. Even if the sequence of steps analyzed here is limited to only three ATA molecules it is expected that the process will be continued beyond the Zr(CL)-ATA-SWCNT interface region, leading to formation of the MOF-CNT heterostructure. The above results obtained under vacuum conditions were further extended to include solvation effects for the case of DMF solvent. The corresponding energy differences with respect to initial configuration are indicated in parentheses for each configuration in Figure 2. Similar to vacuum case and for either of the two sequences of steps, the general trend remains the same under solvation conditions. Specifically, an increase in stability of the intermediate species takes place upon bonding of Zr(CL) with up to three ATA molecules. The only notable difference is the decrease in absolute values of the relative energies indicating smaller interactions among various ligands and Zr cluster or SWCNT systems. Altogether, the results

obtained indicate that SWCNT and its surface defects enhance adsorption of $\rm Zr(CL)$ and ATA molecular precursors, promote interaction among these precursors and ultimately can lead to reacted $\rm Zr(CL,r)$ clusters stabilized at CNT defect sites. In turn such processes allow initiation of the nucleation process of UiO-66-NH₂ MOF directly on SWCNT surface, with particularly strong coupling in proximity of the functionalized defects.

DFT calculations revealed that MOF precursors preferentially interact with the defect sites on ox-SWCNT sidewalls, which increased their local concentration on the surface of ox-SWCNTs. To further inspect the interaction between Zr oxide-cluster and ox-SWCNT defect site, Raman spectroscopy and X-ray photoelectron spectroscopy (XPS) were performed. A mixture consisting of 316 μ L ox-SWCNT stock solution, 1.1 mL Zr oxide-cluster solution and 584 μ L DMF was prepared to match the Zr : ox-SWCNT ratio in following experiments. After stirring for 2 hours, Zr treated ox-SWCNT (hereafter referred to as ox-SWCNT/Zr) was separated by centrifugation and was washed with DMF for 3 times subsequently. The obtained ox-SWCNT/Zr was suspended in 2 mL DMF. Ox-SWCNT stock solution, ox-SWCNT/Zr suspension and Zr oxide-cluster stock solution were drop cast on silicon chips and aluminum tape for Raman and XPS characterization, respectively.

Raman spectra showed a shift of the radial breathing mode (RBM) for ox-SWCNT/Zr and UiO-66-NH₂/ox-SWCNT compared to ox-SWCNT (Figure S6). Typically, RBM shift can be ascribed to multiple factors such as chemical modification, bundle size, temperature, and pressure. Both Zr oxide-cluster and UiO-66-NH₂ shifted the RBM peak to lower wavenumbers, indicative of their functionalization on ox-SWCNT. C 1s and Zr 3d XPS scans were performed for all three samples (Figure S7). Ox-SWCNT/Zr displayed the Zr peaks which were not present in pure ox-SWCNT, thus confirming that the Zr oxide-cluster was anchored onto ox-SWCNT. Notably, the C=O binding energy of ox-SWCNT/Zr shifted to 286.77 eV compared to ox-SWCNT at 288.07 eV. This shift is ascribed to Zr covalently binding at the defect site on ox-SWCNT. The presence of C-O-Zr interaction impaired the intensity of C=O bond on ox-SWCNT, resulting in a shift to lower binding energy.

To leverage these covalent interactions for more heterogeneous growth, the overall precursor concentration was decreased (Table 1, material 2). Material 2 displayed (Figure 3a) a distinctive morphology consisting of a shell-like layer formed on the ox-SWCNTs instead of normal MOF crystalline structure as found in the case of material 1 (Figure S1B). The XRD pattern of material 2 (Figure 3e) had broad peaks corresponding to the simulated bulk UiO-66-NH2 peaks, indicative of the fact that the MOF crystal sizes were small. The resulting MOF shell structure on the ox-SWCNTs cores was comprised of individual UiO-66-NH2 nucleation cores. Their small size indicated that the lowered precursor concentration promoted nucleation over the growth.

Promoting further heterogeneous MOF growth on ox-SWCNT surfaces was pursued by utilizing a syringe pump (SI Experimental section) to impede homogeneous MOF growth. The syringe pump strategy has been recently used in successful syntheses of core-shell gold-nanorod@Zr-MOF composites.²² With one of the MOF precursors introduced gradually into the synthesis, the nucleation

threshold concentration was first reached at the defect sites due to increased local concentrations. Most MOF structures were therefore formed on the nanotube surface instead of in the homogeneous phase. In our syringe pump syntheses, either one of the two MOF precursors were introduced to ox-SWCNTs suspension first while the other precursor was added from a syringe pump over a period of time. Both adding sequences (Table 1, materials 3 and 4) were performed and the results are as follows. When ATA was added from a syringe pump, MOF crystalline beads were observed in the composites (Figure 3b). XRD pattern of material 3 showed characteristic sharp peaks of UiO-66-NH₂ (Figure 3e). TEM observations revealed that almost all the MOF crystals were hybridized with ox-SWCNTs. Single MOF beads on one strand of ox-SWCNTs prove MOF nucleation and growth are occurring from the sidewalls of ox-SWCNT. However, when Zr cluster solution was pumped, the composites shared a similar morphology as material 2 (Figure 3c). The XRD peaks of material 4 were broader than those of material 3, which indicated that crystalline domains in material 4 were smaller.

The noticeable morphology differences resulting from precursor adding sequence revealed another factor controlling the MOF growth. During the two-step UiO-66-NH $_2$ synthesis, acetic acid was added into the Zr solution to form stable Zr oxide-clusters. It was reported that acetic acid controls the MOF crystal size by changing the synthetic kinetics. ²³ In the case of the syringe pump synthesis, when the ATA solution was added from the syringe pump, the acetic acid present already in the Zr solution regulates the reaction. However, when Zr was added gradually, the acetic acid concentration was too low to compete with ATA binding to zirconium oxide-cluster, leading to an uncontrolled nucleation as the reaction initiated.

To investigate the effect of the modulator, control syntheses with additional acetic acid were conducted (Table 1, material 5). When more acetic acid was added into the synthesis, the MOF crystals primarily formed on the ox-SWCNT sidewalls (Figure 3d). As the acetic acid modulator concentration was increased, the MOF ligand exchange in homogeneous phase was inhibited. However, on the sidewalls of ox-SWCNTs, where MOF precursors were pre-concentrated, the MOF nucleation can still happen. Syntheses of materials 6 and 7 were performed with the syringe pump method and an additional amount of acetic acid was introduced. ATA and Zr oxide-cluster were pumped during the synthesis of materials 6 and 7, respectively. Material 6 and 7 have similar morphologies (Figure S4). Both composites have well-defined MOF crystallites on the ox-SWCNTs regardless of the adding sequence. The difference between materials 3 and 4 was therefore attributed to the lack of acetic acid during the synthesis of material 4. When the acetic acid amount was tripled (material 8), the MOF growth was completely stopped and only bare ox-SWCNT bundles can be observed under TEM (Figure S5). XRD analysis indicates no crystal structure formation in the case of material 8 (Figure S5).

A time dependent TEM was performed with material **5** (Figure S8) to shed light on the growth mechanism. No obvious MOF structure but small nucleation spots on ox-SWCNT can be seen until the reaction reached 6 hours. Well-defined UiO-66-NH₂ crystals started to form after 8 hours, afterwards no obvious morphology change was observed. Ox-SWCNT was able to adsorb MOF precursors at early

stage to form MOF nucleation spots and then template the growth of $UiO-66-NH_2$.

As material 5 successfully achieved the desired "beads-on-astring" morphology, additional N2 adsorption-desorption isotherm and electrical measurements were performed for this material. As shown in Figure 4a, material 5 displayed a type-I isotherm, characteristic to microporous solids. Isotherms of pure ox-SWCNT and UiO-66-NH₂ were measured for comparison. The BET surface area was calculated to be 248.7 m² g⁻¹, 1228 m² g⁻¹ and 1266 m² g⁻¹ for ox-SWCNT, material 5 and UiO-66-NH₂, respectively. The surface area of material 5 is close to that of pure UiO-66-NH2. The slight decrease can be attributed to the incorporation of less porous ox-SWCNT in the composites. To test the electrical performance, material 5 was deposited onto a silicon chip with interdigitated gold microelectrodes using DEP to fabricate FET and chemiresistor devices. The current-voltage curve showed that material 5 was electrically conductive (Figure 4b). These experiments indicated that the as-synthesized UiO-66-NH2/ox-SWCNT composite had both the microporosity of MOF and the electrical conductivity of carbon nanotubes. To quantify the conductivity of material 5, the sample was drop cast to fabricate chemiresistor devices where a thick layer of material 5 completely covered the electrode area. The currentvoltage curve of this device displays a conductivity of 0.256 S cm⁻¹ (Figure S9b). The conductivity of drop-cast ox-SWCNT was calculated to be 16.9 S cm⁻¹ in the same manner. Conductivity (σ) was calculated from the following equation:

$$\sigma = \frac{1}{R \times \frac{A}{L}}$$

where R is resistance (8.42 \times 10³ Ω for material **5**), A is area of the electrode (3.25 \times 10⁻⁷ cm²), and L is length of the electrode (7 \times 10⁻⁴ cm).

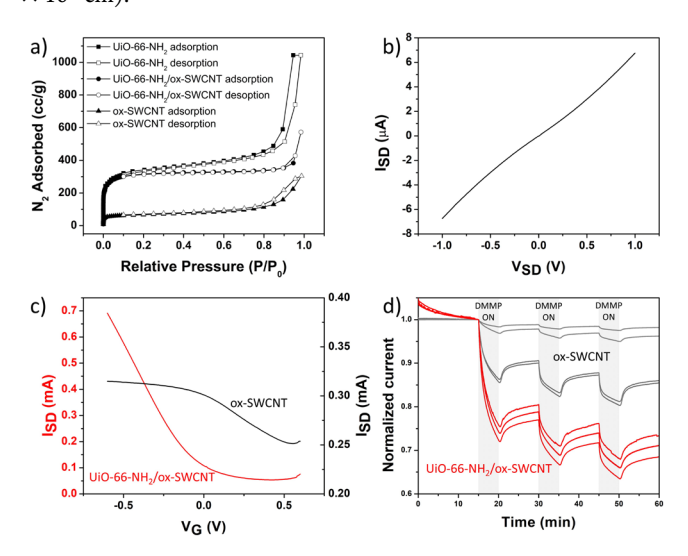


Figure 4. Characterization of UiO-66-NH₂/ox-SWCNT "beads-on-astring" composite (material **5**). a) N₂ adsorption and desorption isotherms at 77 K. b) Source-drain (SD) current-voltage curve. c) Liquid FET characteristics, i.e., source-drain current (I_{SD}) versus gate voltage (V_{G}), UiO-66-NH₂/ox-SWCNT (red) in comparison to ox-SWCNTs (gray). d) Chemiresistor responses (normalized current traces versus time) of ox-SWCNT (gray) and UiO-66-NH₂/ox-SWCNT (red)

devices exposed to three 5-minute cycles of saturated DMMP vapor (light gray shaded rectangle areas).

UiO-66-NH2 has also good stability in water, thus allowing the UiO-66-NH₂/ox-SWCNT composites to be used as potential liquid field-effect-transistor.²⁴ No major loss of crystallinity was observed from PXRD pattern of material 5 after being stored in water for 5 days (Figure S10). Material 5 demonstrated a p-type semiconductor behavior (Figure 4c). The FET curve of material 5 shifted toward more negative gate voltage compared to ox-SWCNT device, which indicates n-doping of SWCNTs after functionalization with UiO-66-NH₂. Individually, both ox-SWCNT and UiO-66-NH₂ have been used as dimethyl methylphosphonate (DMMP) sensing materials in the previous studies. 25,26 Therefore, we explored chemical sensitivity of the synthesized UiO-66-NH₂/ox-SWCNT hybrids toward DMMP vapor. Both the ox-SWCNT and UiO-66-NH₂/ox-SWCNT chemiresistor devices demonstrated a decrease in conductance after exposure to 3 cycles of air saturated with DMMP vapor (Figure 4d). The DMMP concentration in air (0.110 vol%) was estimated following previous studies.²⁷ The response to DMMP vapor was quantified by calculating the relative change in current:

$$Response = \frac{I_{DMMP} - I_{air}}{I_{air}}$$

in which $I_{\rm air}$ and $I_{\rm DMMP}$ are the device current before and after 5 minutes of exposure to DMMP vapor, respectively. The UiO-66-NH₂/ox-SWCNT had an average response value of -16.3% while the ox-SWCNT had an average response of -5.87% (Figure S11). A possible reason for the improved response of UiO-66-NH₂ functionalized ox-SWCNTs is due to the change in the UiO-66-NH₂ work function after exposure to DMMP. It has been reported that parts per billion (ppb) level concentration of DMMP can significantly shift the work function of UiO-66. We contend that this work function shift may further perturb the electrical conductivity of SWCNT, leading to the observed larger response. Admittedly, more work is needed to pinpoint the exact mechanism of the MOF/SWCNT hybrid interactions with the analyte molecules and the electrical signal transduction.

CONCLUSION

In this work, we demonstrated a facile synthesis of UiO-66-NH₂ decoration on the surface of oxidized single-walled carbon nanotubes (ox-SWCNTs). By adding acetic acid, the nucleation of UiO-66-NH₂ was constrained to occur on the surface of ox-SWCNTs heterogeneously instead of homogeneously in solution. The morphology of UiO-66-NH2 was tunable by adjusting the amount of acetic acid present in the synthesis. The MOF displayed a sheet-like structure made up of small crystalline domains at low acetic acid concentration, while moderate acetic acid concentration gave rise to MOF beads on ox-SWCNTs strings. The UiO-66-NH₂/ox-SWCNT composites were shown to combine the porous property of UiO-66-NH₂ MOF and the electrically conductive property of ox-SWCNTs. DFT calculations and XPS revealed that the carboxyl defect sites were essential for the MOF/CNT hybridization. The MOF precursors tended to adsorb near the defect sites and induce the heterogeneous MOF nucleation. Such covalent bonding between ox-SWCNTs and MOF precursors provides a general synthetic method to hybridize

carboxylate type MOFs with ox-SWCNTs and prepare electrically conductive MOF composites.

ASSOCIATED CONTENT

Supporting Information. Additional experimental details, computational details, TEM images, XRD patterns, adsorption heat. (PDF). This material is available free of charge via the Internet at http://pubs.acs.org.

AUTHOR INFORMATION

Corresponding Author

Alexander Star: astar@pitt.edu

Author Contributions

The manuscript was written through contributions of all authors. All authors have given approval to the final version of the manuscript.

Funding Sources

The work at University of Pittsburgh was supported by the National Science Foundation under Grant No. 2003302.

Notes

The authors declare no competing financial interests.

ACKNOWLEDGMENT

We thank the Department of Biological Science and Nanoscale Fabrication and Characterization Facility (NFCF) at the University of Pittsburgh for access to the TEM and XRD instrumentation.

ABBREVIATIONS

SWCNT, single-walled carbon nanotube; MWCNT, multi-walled carbon nanotube; ox-SWCNT, oxidized single-walled carbon nanotube; CNT, carbon nanotube; DMMP, dimethyl methylphosphonate; ATA, 2-aminoterephthalic acid; DFT, density function theory; Zr(CL), $Zr_6O_4(OH_4)(CH_3COO)_{12}$ cluster; AA. Acetic acid.

REFERENCES

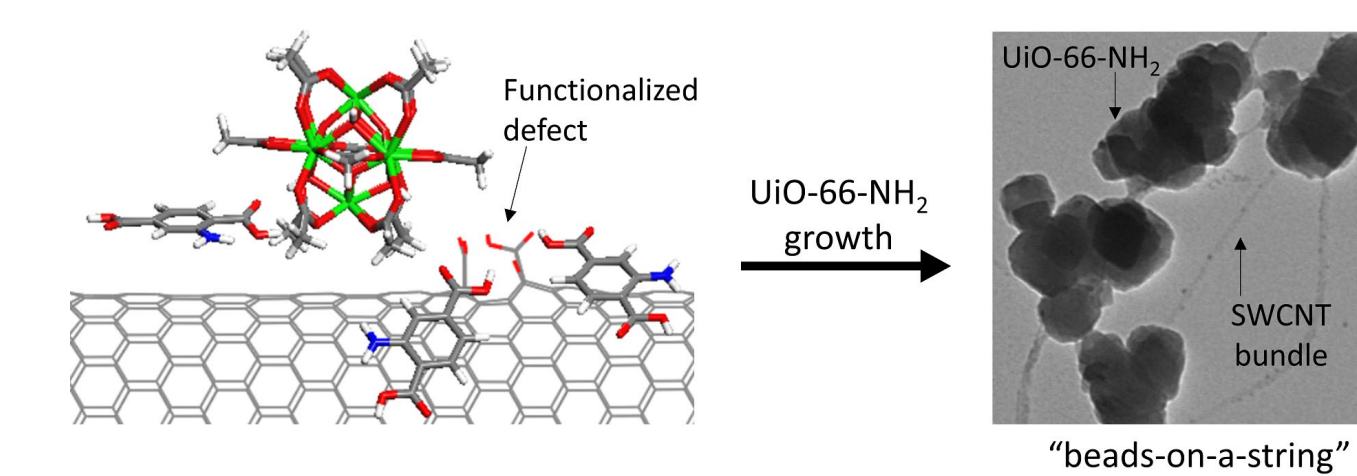
- 1. Furukawa, H.; Cordova, K. E.; O'Keeffe, M.; Yaghi, O. M., The Chemistry and Applications of Metal-Organic Frameworks. *Science* **2013**, *341* (6149), 1230444.
- 2. Sun, L.; Campbell, M. G.; Dinca, M., Electrically Conductive Porous Metal-Organic Frameworks. *Angew. Chem., Int. Ed.* **2016**, *55* (11), 3566-79.
- 3. Xie, L. S.; Skorupskii, G.; Dincă, M., Electrically Conductive Metal-Organic Frameworks. *Chem. Rev.* **2020**, *120* (16), 8536-8580.
- 4. Yoo, J.; Lee, S.; Lee, C. K.; Kim, C.; Fujigaya, T.; Park, H. J.; Nakashima, N.; Shim, J. K., Homogeneous Decoration of Zeolitic Imidazolate Framework-8 (ZIF-8) with Core–Shell Structures on Carbon Nanotubes. *RSC Adv.* **2014**, *4* (91), 49614-49619.
- 5. Sohrabi, S.; Dehghanpour, S.; Ghalkhani, M., A Cobalt Porphyrin-Based Metal Organic Framework/Multi-Walled Carbon Nanotube Composite Electrocatalyst for Oxygen Reduction and Evolution Reactions. *J. Mater. Sci.* **2017**, *53* (5), 3624-3639.
- 6. Wang, Q.; Wang, Q.; Xu, B.; Gao, F.; Gao, F.; Zhao, C., Flower-Shaped Multiwalled Carbon Nanotubes@Nickel-Trimesic Acid MOF Composite as a High-Performance Cathode Material for Energy Storage. *Electrochim. Acta* **2018**, 281, 69-77.
- 7. Zhang, H.; Zhao, W.; Zou, M.; Wang, Y.; Chen, Y.; Xu, L.; Wu, H.; Cao, A., 3D, Mutually Embedded MOF@Carbon Nanotube Hybrid Networks for High-Performance Lithium-Sulfur Batteries. *Adv. Energy Mater.* **2018**, 8 (19).

 8. Pu. Y.; Wu, W.; Liu, L.; Liu, T.; Ding, F.; Zhang, L.; Tang, Z., A
- 8. Pu, Y.; Wu, W.; Liu, J.; Liu, T.; Ding, F.; Zhang, J.; Tang, Z., A Defective MOF Architecture Threaded by Interlaced Carbon Nanotubes for High-Cycling Lithium—Sulfur Batteries. RSC Adv. 2018, 8 (33), 18604-18612.

- 9. Wang, Y.-S.; Chen, Y.-C.; Li, J.-H.; Kung, C.-W., Toward Metal-Organic-Framework-Based Supercapacitors: Room-Temperature Synthesis of Electrically Conducting MOF-Based Nanocomposites Decorated with Redox-Active Manganese. *Eur. J. Inorg. Chem.* **2019**, 2019 (26), 3036-3044.
- 10. Li, Y.; Ye, W.; Cui, Y.; Li, B.; Yang, Y.; Qian, G., A Metal-Organic Frameworks@ Carbon Nanotubes Based Electrochemical Sensor for Highly Sensitive and Selective Determination of Ascorbic Acid. *J. Mol. Struct.* **2020**, 1209.
- 11. Prasanth, K. P.; Rallapalli, P.; Raj, M. C.; Bajaj, H. C.; Jasra, R. V., Enhanced Hydrogen Sorption in Single Walled Carbon Nanotube Incorporated MIL-101 Composite Metal–Organic Framework. *Int. J. Hydrogen Energy* **2011**, 36 (13), 7594-7601.
- 12. Cortes-Suarez, J.; Celis-Arias, V.; Beltran, H. I.; Tejeda-Cruz, A.; Ibarra, I. A.; Romero-Ibarra, J. E.; Sanchez-Gonzalez, E.; Loera-Serna, S., Synthesis and Characterization of an SWCNT@HKUST-1 Composite: Enhancing the CO₂ Adsorption Properties of HKUST-1. *ACS Omega* **2019**, 4 (3), 5275-5282.
- 13. Kim, S. N.; Rusling, J. F.; Papadimitrakopoulos, F., Carbon Nanotubes for Electronic and Electrochemical Detection of Biomolecules. *Adv. Mater.* **2007**, *19* (20), 3214-3228.
- 14. Schroeder, V.; Savagatrup, S.; He, M.; Lin, S.; Swager, T. M., Carbon Nanotube Chemical Sensors. *Chem. Rev.* **2019**, *119* (1), 599-663.
- 15. Ellis, J. E.; Zeng, Z.; Hwang, S. I.; Li, S.; Luo, T. Y.; Burkert, S. C.; White, D. L.; Rosi, N. L.; Gassensmith, J. J.; Star, A., Growth of ZIF-8 on Molecularly Ordered 2-Methylimidazole/Single-Walled Carbon Nanotubes to Form Highly Porous, Electrically Conductive Composites. *Chem. Sci.* **2019**, *10* (3), 737-742.
- 16. Jiang, Y.; Liu, C.; Caro, J.; Huang, A., A New UiO-66-NH₂ Based Mixed-Matrix Membranes with High CO₂/CH₄ Separation Performance. *Microporous Mesoporous Mater.* **2019**, 274, 203-211.
- 17. Peterson, G. W.; Mahle, J. J.; DeCoste, J. B.; Gordon, W. O.; Rossin, J. A., Extraordinary NO₂ Removal by the Metal-Organic Framework UiO-66-NH₂. Angew. Chem., Int. Ed. **2016**, 55 (21), 6235-8.
- 18. Sang, X.; Zha, Q.; Nie, X.; Liu, D.; Guo, Y.; Shi, X.; Ni, C., Interfacial Growth of Metal–Organic Framework on Carboxyl-Functionalized Carbon Nanotubes for Efficient Dye Adsorption and Separation. *Anal. Methods* **2020**, *12* (37), 4534-4540.
- 19. Sun, X.; Chen, Y.; Xie, Y.; Wang, L.; Wang, Y.; Hu, X., Preparation of a Chemically Stable Metal–Organic Framework and Multi-Walled Carbon Nanotube Composite as a High-Performance Electrocatalyst for the Detection of Lead. *Analyst* **2020**, *145* (5), 1833-1840.
- 20. DeStefano, M. R.; Islamoglu, T.; Hupp, J. T.; Farha, O. K., Room-Temperature Synthesis of UiO-66 and Thermal Modulation of Densities of Defect Sites. *Chem. Mater.* **2017**, *29* (3), 1357-1361.
- 21. Graupner, R., Raman Spectroscopy of Covalently Functionalizaed Single-Wall Carbon Nanotubes. *J. Raman Spectrosc.* **2007**, 673-683.
- 22. Osterrieth, J. W.; Wright, D.; Noh, H.; Kung, C.-W.; Vulpe, D.; Li, A.; Park, J. E.; Van Duyne, R. P.; Moghadam, P. Z.; Baumberg, J. J., Core–Shell Gold Nanorod@ Zirconium-Based Metal–Organic Framework Composites as in Situ Size-Selective Raman Probes. J. Am. Chem. Soc. 2019, 141 (9), 3893-3900.
- 23. Gu, Y.; Xie, D.; Ma, Y.; Qin, W.; Zhang, H.; Wang, G.; Zhang, Y.; Zhao, H., Size Modulation of Zirconium-Based Metal Organic Frameworks for Highly Efficient Phosphate Remediation. ACS Appl. Mater. Interfaces 2017, 9 (37), 32151-32160.
- 24. Kandiah, M.; Nilsen, M. H.; Usseglio, S.; Jakobsen, S.; Olsbye, U.; Tilset, M.; Larabi, C.; Quadrelli, E. A.; Bonino, F.; Lillerud, K. P., Synthesis and Stability of Tagged UiO-66 Zr-MOFs. *Chem. Mater.* **2010**, 22 (24), 6632-6640.
- 25. Wang, Y.; Zhou, Z.; Yang, Z.; Chen, X.; Xu, D.; Zhang, Y., Gas Sensors Based on Deposited Single-Walled Carbon Nanotube Networks for DMMP Detection. *Nanotechnology* **2009**, *20* (34), 345502.
- 26. Stassen, I.; Bueken, B.; Reinsch, H.; Oudenhoven, J. F. M.; Wouters, D.; Hajek, J.; Van Speybroeck, V.; Stock, N.; Vereecken, P. M.; Van Schaijk, R.; De Vos, D.; Ameloot, R., Towards Metal–Organic Framework Based Field Effect Chemical Sensors: UiO-66-NH₂ for Nerve Agent Setection. *Chem. Sci.* **2016**, 7 (9), 5827-5832.

27. Butrow, A. B.; Buchanan, J. H.; Tevault, D. E., Vapor Pressure of Organophosphorus Nerve Agent Simulant Compounds. *J. Chem. Eng. Data* **2009**, 54 (6), 1876-1883.

Table of Contents



composites